

TURBULENT RECONNECTION IN RELATIVISTIC PLASMAS AND EFFECTS OF COMPRESSIBILITY

MAKOTO TAKAMOTO

Max-Planck-Institut für Kernphysik, Heidelberg, Germany and
Department of Earth and Planetary Science, The University of Tokyo, Japan

TSUYOSHI INOUE

Division of Theoretical Astronomy, National Astronomical Observatory of Japan

ALEXANDRE LAZARIAN

Department of Astronomy, University of Wisconsin, 475 North Charter Street, Madison, WI 53706, USA
Draft version October 26, 2015

ABSTRACT

We report turbulence effects on magnetic reconnection in relativistic plasmas using 3-dimensional relativistic resistive magnetohydrodynamics simulations. We found reconnection rate became independent of the plasma resistivity due to turbulence effects similarly to non-relativistic cases. We also found compressible turbulence effects modified the turbulent reconnection rate predicted in non-relativistic incompressible plasmas; The reconnection rate saturates and even decays as the injected velocity approaches to the Alfvén velocity. Our results indicate the compressibility cannot be neglected when compressible component becomes about half of incompressible mode occurring when the Alfvén Mach number reaches about 0.3. The obtained maximum reconnection rate is around 0.05 to 0.1, which will be able to reach around 0.1 to 0.2 if injection scales are comparable to the sheet length.

Subject headings: magnetic fields, magnetohydrodynamics (MHD), magnetic reconnection, relativistic processes, plasmas, turbulence

1. INTRODUCTION

Magnetic reconnection is known as a process responsible for a very efficient magnetic field dissipation in many plasma phenomena. In particular, it is expected to play an important role for the acceleration of relativistic outflow in high energy astrophysical phenomena accompanying Poynting-dominated plasmas, such as relativistic jets (Blandford & Znajek 1977; Begelman et al. 1984; Komissarov et al. 2007; Kino et al. 2015), pulsar wind (Kennel & Coroniti 1984a,b; Lyubarsky & Kirk 2001; Kirk & Skjæraasen 2003), and gamma-ray bursts (GRB) (Lyutikov & Blandford 2003; Zhang & Yan 2011). However, the classical theory of magnetic reconnection (Sweet 1958; Parker 1957) predicts that magnetic reconnection becomes very slow in high magnetic Reynolds number plasmas ($R_m \sim 10^{10}$), and fails to explain observed dissipation timescale in space and astrophysical phenomena. To solve this problem, a lot of efforts have gone into finding a *fast-reconnection* process that does not depend on the value of resistivity. Using the equation of continuity, the reconnection rate can be expressed as

$$\frac{v_{\text{in}}}{c_A} = \frac{\rho_s}{\rho_{\text{in}}} \frac{v_s}{c_A} \frac{\delta}{L}, \quad (1)$$

where the subscript “in” and “s” indicate the inflow and outflow region, respectively, v_{in} , v_s are the inflow and outflow velocity, respectively, c_A is the Alfvén velocity, ρ is the mass density, δ is the sheet thickness, and L is the sheet length. This equation shows that fast reconnection processes can be obtained by increasing the density ratio: ρ_s/ρ_{in} , (Brunel

et al. 1982), the outflow velocity: v_s/c_A , and the aspect ratio of sheets: δ/L (Biskamp 1986; Shibata & Tanuma 2001; Loureiro et al. 2007; Bhattacharjee et al. 2009; Uzdensky et al. 2010; Takamoto 2013; Sironi & Spitkovsky 2014).

Turbulence has been considered as a key process that can accelerate magnetic field annihilation (Matthaeus & Lamkin 1985; Eyink 2011; Takamoto et al. 2012; Higashimori et al. 2013). In particular, many astrophysical objects are considered to be high Reynolds number plasma, and it is natural to assume those plasma are in a turbulent state¹. It was theoretically suggested that strong Alfvénic turbulence also increases the sheet aspect ratio, and the reconnection rate becomes independent of the resistivity (Lazarian & Vishniac (1999), henceforth LV99). LV99 predicts the following expression of reconnection rate:

$$\frac{v_{\text{in}}}{c_A} \simeq \min \left[\left(\frac{L}{l} \right)^{1/2}, \left(\frac{l}{L} \right)^{1/2} \right] \left(\frac{v_l}{c_A} \right)^2 \quad (2)$$

where l and v_l are the energy injection scale and velocity dispersion of turbulence at the injection scale, respectively. This was examined using magnetohydrodynamics (MHD) simulation (Kowal et al. 2009). However, the numerical work was limited only in the non-relativistic incompressible regime with plasma β larger than unity, and its applicability to relativistic Poynting dominated plasma with relativistic turbu-

¹ In Poynting dominated plasmas, relatively strong turbulence may be able to be induced by various ways, e.g., Kruskal-Schwarzschild type instability (Lyubarsky 2010) and Richtmyer-Meshkov type instability (Inoue 2012) at a shock front, which induces turbulence with velocity dispersion up to $\Delta v_{\text{turb}}/a \lesssim 1.5/\sqrt{\sigma}$ (Takamoto et al. 2012); the tearing instability with turbulent velocity Lorentz factor, $\gamma_{\text{turb}} \simeq \sqrt{\alpha\sigma/2}$, where σ is the magnetization parameter defined later, a is the sound velocity, and α is energy conversion factor from magnetic field into kinetic energy.

lence was unclear, which is very important in the context of high energy astrophysical phenomena (Lyutikov & Lazarian 2013; Kadowaki et al. 2015).

In this paper, we extend the previous work to relativistic plasma including both matter and Poynting dominated plasma. We also investigate effects from compressibility on reconnection rate. In Section 2 we introduce the numerical setup and the method for the turbulence injection. The numerical result is presented in Section 3, and its theoretical explanation is presented in Section 4. Their implications for some high energy astrophysical phenomena are discussed in Section 5. Section 6 summarizes our conclusions.

2. SIMULATION SETUP

We modelled the evolution of a current sheet in a turbulent flow using 3-dimensional resistive relativistic magnetohydrodynamics (RRMHD). The initial current sheet is modelled by the relativistic Harris sheet (Hoh 1966; Kirk & Skjæraasen 2003) whose magnetic field is expressed as

$$\mathbf{B} = B_0 \tanh[z/\lambda] \mathbf{e}_x + B_G \mathbf{e}_y, \quad (3)$$

where λ is the half-thickness of the initial sheet, and B_0 and B_G are the reconnecting magnetic field and guide field component, respectively. The pressure inside of the sheet is assumed to satisfy the pressure balance, and the upstream pressure is determined by the magnetization parameter $\sigma \equiv B^2/4\pi\rho hc^2$ where $h = 1 + (\Gamma/(\Gamma-1))(p/\rho c^2)$ is the specific enthalpy of relativistic ideal gas with $\Gamma = 4/3$, and p, ρ, c are the gas pressure, mass density, and the light velocity, respectively. The initial temperature is assumed uniform, $\Theta \equiv k_B T/mc^2 = 1$, where k_B, m are the Boltzmann constant and particle rest mass, respectively.

The evolution of the plasma is calculated using a 3-dimensional RRMHD scheme developed by Takamoto & Inoue (2011) which solves the full RRMHD equations in a conservative fashion using the constrained transport algorithm. This allows us to treat the mass density, momentum, energy, and divergence of magnetic field to be conserved within machine round-off error. The resistivity, η , was assumed to be constant, typically $\eta/Lc = 10^{-4}$. We followed the similar simulation setup used in Kowal et al. (2009). The numerical box is assumed $[-L/2, L/2] \times [0, L] \times [-L, L]$ where $L = 20\lambda^2$. Note that the z-direction size of the numerical box is twice larger than x, y-direction to reduce the influence by turbulence on the reconnection inflow around z-boundaries. We divided the numerical box into the homogeneous numerical cells with size: $\Delta = L/512$. The timestep size is set as: $\Delta t = 0.1\Delta/c$. We set the periodic boundary condition in y-direction and free boundary condition x and z-direction.

In our model, we drive turbulence using a similar method described by Mac Low (1999). We add a divergence-free 3-velocity field, $\delta\mathbf{v}$, and an electric field determined consistently to the injected velocity³ at time intervals Δt_{inj} in a box region located around the current sheet: $[-l_x, l_x] \times [0, L] \times [-l_z, l_z]$ where l_x, l_z are a scale length that is sufficiently larger than the injected turbulence eddy scale; Δt_{inj} is chosen to be shorter than the eddy turnover time at the injection scale l : $\Delta t_{\text{inj}} = l/4\pi v_{\text{inj},0}$ where $v_{\text{inj},0} = 0.15c$ is a typical injection velocity in this study. We note that the dynamics of

² Note that λ is the *initial* half-width of the sheet, and is a constant.

³ First, we splitted the electric field as: $\vec{E} = \vec{E}_{\text{dissip}} - \vec{v} \times \vec{B}$. Then, the ideal part is replaced by $\delta\vec{E} = -\vec{v}_{\text{new}} \times \vec{B}$ where \vec{v}_{new} is obtained by the relativistic addition law of \vec{v} and $\delta\vec{v}$.

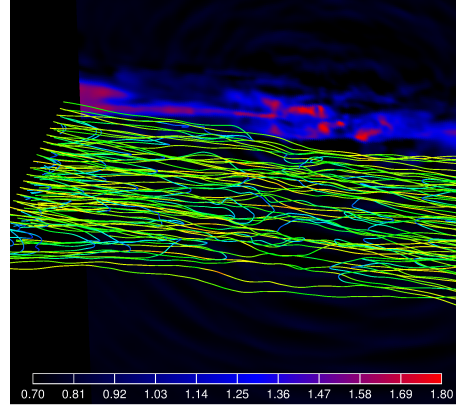


Figure 1. The profile of magnetic field lines in a turbulent sheet and the gas pressure (back plane) in the case of $\sigma = 5$. The color bar is the gas pressure in the unit of the magnetic pressure in the initial inflow region.

the turbulence becomes insensitive to the injection time interval as long as the injection time interval is around the eddy turnover time at the injection scale. Following (Inoue et al. 2011) and (Takamoto et al. 2012), the velocity field is described as: $\gamma\delta v^i = \sum_{\vec{k}} P(k) \sin(\vec{k} \cdot \vec{x} + \phi_k^i)$ where γ is the Lorentz factor of the injected velocity, i covers $\{x, y, z\}$, and ϕ_k^i is a random phase. The one-dimensional power spectrum of the velocity field is assumed flat, $k^2 P(k) \propto k^0$. The initial-field perpendicular Fourier components $k_{\perp} = \sqrt{k_y^2 + k_z^2}$ are chosen in a shell extending from $k_l - \Delta k$ to $k_l + \Delta k$ where $k_l L/2\pi = 16, \Delta k L/2\pi = 3$. Note that this scale size is a little larger than the initial sheet scale, and can be well-resolved by our present resolution. The parallel-field wave number $k_{\parallel} = k_x$ is determined by $k_{\parallel} = k_{\perp} v_{\text{inj}}/c_A$ where $v_{\text{inj}} = \sqrt{\langle \delta v^2 \rangle}$ is the root-mean-square velocity. Since the injected turbulent velocity does not immediately follow the critical balance condition (Goldreich & Sridhar 1995), the turbulence at the injected scale is weak (Galtier et al. 2000), which transits into the strong turbulence around the sheet width scale because of the energy cascade (Perez & Boldyrev 2008; Verdini & Grappin 2012; Meyrand et al. 2015). The weak MHD turbulence cascades the wave energy only perpendicular to the magnetic field, the turbulence strength, $\chi \equiv \tau_A/\tau_{\text{NL}} \simeq k_{\perp} v_{\lambda}/k_{\parallel} c_A$, gradually increases up to unity, which results in the strong turbulence in the sheet (Verdini & Grappin 2012; Meyrand et al. 2015). Note that the *injected* velocity v_{inj} is different from the velocity *at the injection scale* v_l , which was first pointed out in LV99. At the injection scale, the weak MHD turbulence theory gives the following the energy cascade rate: $\epsilon_{\text{inj}} \sim v_l^2/\tau_{\text{NL}} \sim v_l^4 l_{\parallel}/l_{\perp}^2 c_A$ where $\tau_{\text{NL}} \sim (l_{\perp}/v_l)^2/(l_{\parallel}/c_A)$ is the distortion time of Alfvén wave packets. Combining this to the injected power: $v_{\text{inj}}^2/\Delta t_{\text{inj}}$, we obtain

$$v_{\text{inj}} \gtrsim \sqrt{\frac{\Delta t_{\text{inj}} l_{\parallel}}{c_A l_{\perp}^2}} v_l^2 \propto v_l^2, \quad (4)$$

where the inequality resulted from the excitation of compression modes. In other words, v_{inj} is related to the injected power by some external force or free energy; on the other hand, v_l is the velocity resulted from the energy cascade of the weak MHD turbulence. We observed this relation in our simulations, and assume this in the following (see also (Lazarian & Vishniac 1999; Kowal et al. 2009)).

3. RESULTS

Figure 1 is a snapshot of the gas pressure and magnetic field lines in the case of highly magnetized case: $\sigma = 5$. Differently from the Sweet-Parker sheet, the sheet is highly stochastic due to the turbulence, which induces a lot of reconnection points in the sheet and drives a fast reconnection process. Figures 2 are the observed reconnection rates v_R which is measured using a method proposed by Kowal et al. (2009) (see Equation (13) in this paper); this allows us to measure the effective value of E_y/B_0 in the 3-dimensional case, which provides us a reconnection inflow velocity less contaminated by turbulent flows than the direct measure of inflow velocity, v_z^4 . The top panel shows the reconnection rate with respect to the injected turbulent velocity in various kinds of magnetized plasmas. This shows that the turbulent reconnection rate shows 3 characteristic behaviors depending on the injected turbulent velocity v_{inj}/c_A : (1) increasing region following LV99; (2) saturation region giving maximum rate; (3) decreasing region. When the injected turbulent velocity is sufficiently small, incompressible approximation can be applied, and the reconnection rate grows following Equation (2). On the other hand, when injected velocity becomes comparable to the Alfvén velocity, turbulence becomes compressible and the reconnection rate deviates from the incompressible theory. Interestingly, the injection velocity v_{inj}/c_A at the maximum rate becomes smaller as the magnetization parameter increases. We will discuss the relation of this tendency to the compressible effects in the next section. Note that the error bar in the panel seems decreasing with σ . We consider this is because the kinetic energy of turbulence becomes smaller comparing with the magnetic field energy as the magnetization parameter σ increases. The bottom panel of Figure 2 is the reconnection rate with respect to the different Lundquist number. It shows the reconnection rate is independent of the Lundquist number, and determined by the turbulent strength. Note that the obtained maximum reconnection rate is very fast, $v_R/c_A \sim 0.05$, and even comparable to the relativistic Petschek reconnection rate (Lyubarsky 2005). This maximum reconnection rate also indicate that it will be possible to reach around 0.1 to 0.2 if injection scales are comparable to the sheet length as indicated by Equation (2)⁵.

Figure 3 is the guide field dependence of reconnection rate in the case of $\Delta v_{inj} = 0.15c_A$ and $\sigma_R = 5$ where σ_R is the magnetization parameter determined by reconnecting magnetic field component B_0 . We fixed the reconnected magnetic field and added the guide field component. As was reported by Kowal et al. (2009), the reconnection rate becomes independent of the guide field strength even in a relativistic Poynting-dominated plasma. In the case of $B_G/B_0 = 1$, the time scale necessary for reaching the steady state becomes 5 times longer than no guide field case.

4. THEORETICAL CONSIDERATIONS

4.1. Sheet Density

The obtained reconnection rate in Figure 2 shows an interesting behavior owing to compressibility which cannot be explained by incompressible theory, Equation (2). In the follow-

⁴ In the following, the reconnection rate v_R obtained using the method by Kowal et al (2009) is identified by the reconnection inflow velocity v_{in} , which becomes valid in a statistically steady state because $|E_y| \simeq v_{in} B_0$ in this case.

⁵ Unfortunately, the dependence on the injection scale l is hard to test because of the limited inertial range of turbulence in the simulation.

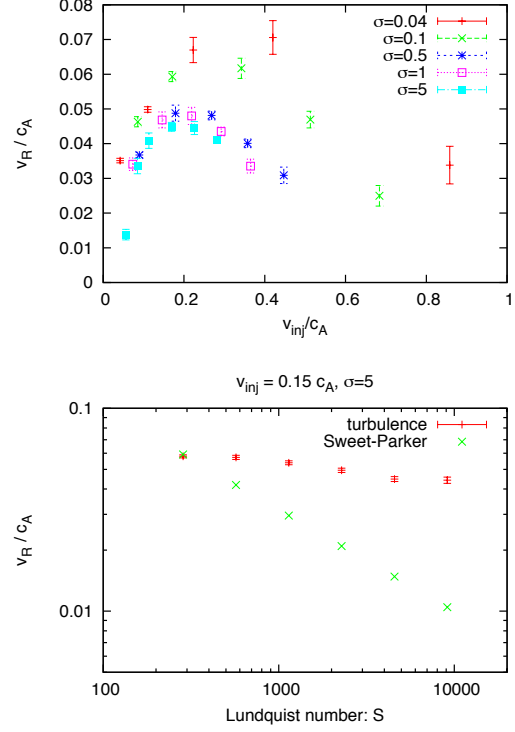


Figure 2. Observed reconnection rate in its steady state. Top: Reconnection rate with respect to the injected turbulent velocity. Bottom: Reconnection rate with respect to the Lundquist number: $S \equiv L c_A / \eta$.

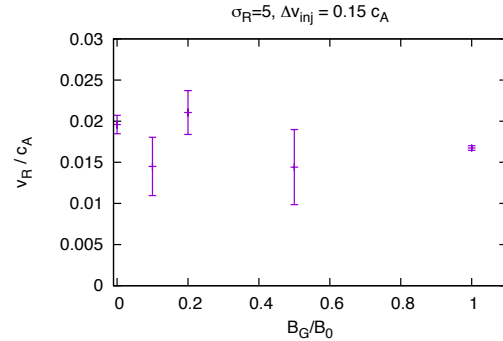


Figure 3. Observed reconnection rate in its steady state with respect to the guide field. Note that the guide field is added to the fixed reconnection field, B_x , so that the total magnetization parameter increases with the guide field.

ing, we give an explanation for the saturation and depression of the reconnection rate in high Alfvén Mach number regime. Equation (1) indicates the compressible effects can be divided into 2 parts: (1) the density ratio between sheet and inflow region ρ_s/ρ_{in} ; (2) decrease of the sheet width δ/L . Note that δ is the actual sheet thickness determined by the turbulence which is different from the initial thickness λ .

We begin with discussing the density ratio. Figure 4 plots ρ_s/ρ_{in} with respect to the injected turbulence velocity in the matter and Poynting dominated cases $\sigma = 0.04$ and 5, respectively. They show that the density ratio decreases linearly with the turbulent strength. This can be understood from the con-

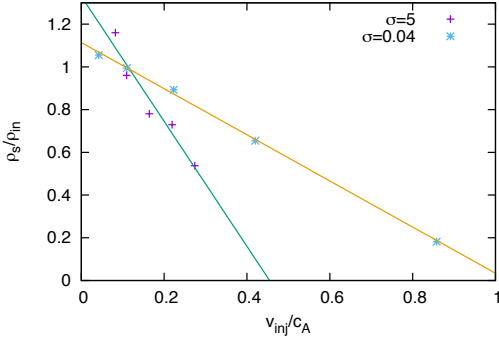


Figure 4. The density ratio between that of inflow and sheet region: ρ_s/ρ_{in} in the cases of Poynting dominated case: $\sigma = 5$ and matter dominated case: $\sigma = 0.04$. The ratio decreases with increasing the turbulent strength due to the compressible effect.

servation of energy flux:

$$\begin{aligned} \rho_{in} h_{in} c^2 (1 + \sigma) v_{in} L + \rho_{in} (1 + 2h_{in} \sigma) \epsilon_{inj} l_x l_z \\ = \left(\rho_s h_s c^2 \gamma_s^2 + \frac{B_s^2}{4\pi} \right) v_s \delta. \end{aligned} \quad (5)$$

We assumed a non-relativistic inflow, $\gamma_{in} = 1$. The 1st and 3rd terms are the energy flux in the inflow and outflow region, respectively. Note that the 2nd term in left-hand side of the equation expresses kinetic and electric field energy of the injected turbulence; The turbulent components in the sheet is neglected because we use a sub-Alfvénic turbulence whose kinetic energy is small compared with the other terms. Using the pressure balance: $p_s = p_{in} + B_{in}^2/8\pi\gamma_{in}^2$, the steady state condition: $cE_y = B_{in}v_{in} = B_s v_s$, and the equation of continuity, Equation (1), we obtain

$$\frac{\rho_s}{\rho_{in}} = \frac{(2h_{in}\sigma + 4\Theta)\gamma_s}{h_{in}(1 + \sigma) - \gamma_s} \left[1 - \frac{1 + 2h_{in}\sigma}{(2h_{in}\sigma + 4\Theta)\gamma_s^2} \frac{\epsilon_{inj}}{\delta} \frac{l_x l_z}{v_s c^2} \right], \quad (6)$$

where we neglected a small term proportional to $(\delta/L)^2 \ll 1$ resulting from $B_s^2/4\pi$. Note that the denominator, $h_{in}(1 + \sigma) - \gamma_s$, is always positive because $\gamma_s \lesssim \gamma_A = \sqrt{1 + \sigma}$ where γ_A is the Lorentz factor of the Alfvén velocity in the upstream region. Since LV99 predicts $\delta \propto L(v_{inj}/c_A)$ (see Equations (2) and (4)), the second term in Equation (6) becomes proportional to: $\epsilon_{inj}/Lv_{inj} \propto v_{inj}$; And we finally obtain the following form of relation: $\rho_s/\rho_{in} = \alpha(1 - \beta v_{inj}/c_A)$ which qualitatively reproduces the linear dependence of the density ratio on the injected turbulence strength v_{inj} in Figure 4⁶.

This decrease of the sheet density can be explained as follows. When the turbulence energy injection rate is small, $v_{inj} \ll c_A$, it increases the sheet width as predicted by LV99. However, the increase of the sheet width is proportional to $|v_{inj}| \propto \epsilon_{inj}^{1/2}$, and the turbulence energy injection rate ϵ_{inj} cannot be absorbed into the sheet width expansion as indicated by the second term in Equation (5). In this case, in order to keep the energy flux conservation, the system reduces the inflow

⁶ Our simulation results did not reproduce the exact value of α and β indicated by Equation (6). However, the obtained values of α roughly reproduced the predicted value by Equation (6), and our results also reproduced the increasing nature of α and β in terms of σ parameter; this is indicated by Equation (6) with an assumption $v_s \sim c_A$ if $v_s < 0.3c$ otherwise $v_s = 0.3c$ which is a known result for relativistic Sweet-Parker sheet (Takahashi et al. 2011). Concerning β , note that it is difficult to estimate the exact value from simulation results because of the uncertainty of l_x, l_z, δ .

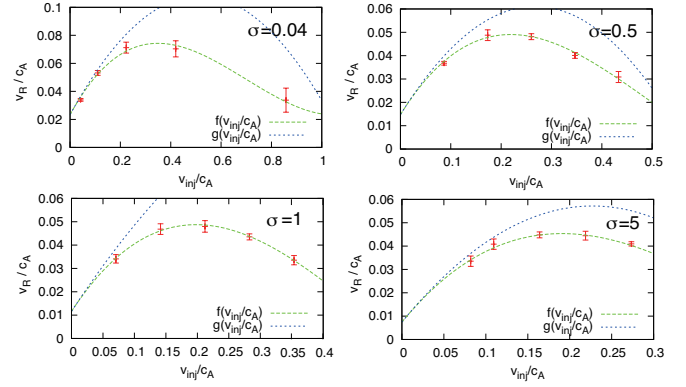


Figure 5. Reconnection rates fitted by two functions: $f(v_{inj}/c_A) = C_1(\rho_s/\rho_{in})[v_{inj}/c_A - C_2(v_{inj}/c_A)^2]$, $g(v_{inj}/c_A) = C_1(\rho_s/\rho_{in})v_{inj}/c_A$. The function f can explain the reconnection rate from the matter dominated case to the Poynting dominated case, which indicates the compressible effects definitely affect the reconnection rate in turbulence. velocity v_{in} in the left-hand side of Equation (5), and this results in the decrease of the sheet density comparing with the inflow density as indicated in Equation (1). In other words, this is because the second term in the left-hand side increases with ϵ_{inj} but right-hand side only increases with $\delta \propto \epsilon_{inj}^{1/2}$. Hence, to keep the energy flux conservation, the system reduces the inflow velocity v_{in} in the left-hand side of Equation (5), and this results in the decrease of the sheet density comparing with the inflow density as indicated in Equation (1).

Note that Equation (6) indicates the density in sheets becomes negative when a too strong turbulence is injected, which does not occur in real situations. This is prohibited by including neglected terms in Equation (5). In particular, as is discussed in Section 4.2, energy flux escaping as compressible waves cannot be neglected as the injected turbulent Alfvén Mach number approaches unity.

4.2. Compressible Turbulence Effects

Next, LV99 obtained the following relation: $\delta/L \propto (v_l/c_A)^2 \propto v_{inj}/c_A$ using the incompressible MHD turbulence cascade law. In this paper, we treated compressible MHD turbulence, so that it is expected the above relation should be modified. More precisely, the LV99's relation can be rewritten as:

$$\frac{\delta}{L} \sim \left(\frac{2\epsilon_{inj}l}{c_A^3} \right)^{1/2} \min \left[\left(\frac{L}{l} \right)^{1/2}, \left(\frac{l}{L} \right)^{1/2} \right], \quad (7)$$

and substituting, $\epsilon_{inj} \sim v_l^4/2lc_A$, recovers Equation (2). Hence, if we find an expression of the energy injection rate ϵ_{inj} including compressible effects, Equation (7) may give us a new expression of the sheet width. Recently, Banerjee & Galtier (2013) obtained an exact relation of energy cascade rate in the non-relativistic isothermal MHD turbulence. In the strong background average magnetic field limit, the relation reduces to:

$$-4\epsilon = \nabla \cdot \vec{F} + B_0^2 S \quad (8)$$

where the divergence ∇ is performed on the correlation length which plays a role of the eddy scale length, \vec{F} is the energy flux vector including compressible effects with order of B_0^2 , and S is a source or sink term due to the compressible effects. This indicates that the compressible effects cannot be

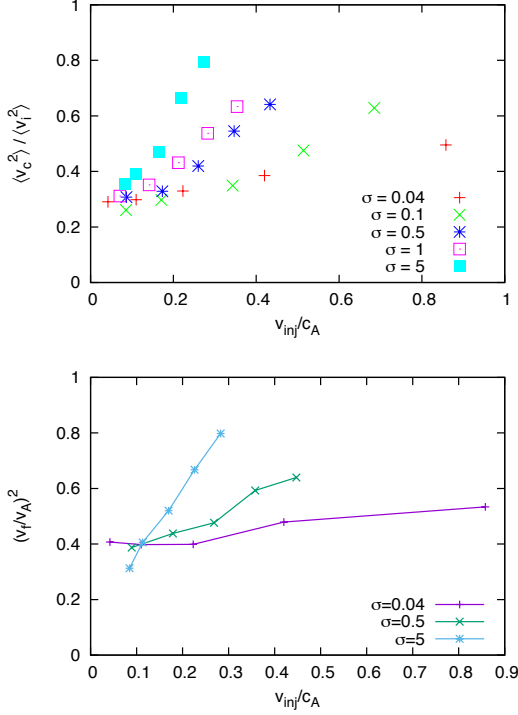


Figure 6. Top: The ratio of the compressible and incompressible velocity components: $\langle v_c^2 \rangle$ and $\langle v_i^2 \rangle$, respectively. Bottom: The ratio of the fast MHD wave and Alfvén wave power: $(V_f/V_A)^2$. The data were calculated by the background without sheet to avoid inhomogeneous background and back reaction from the sheet. The panel shows the ratio with respect to the strength of the injected turbulence: v_{inj}/c_A with various kinds of the magnetization parameter.

neglected in the strong background magnetic field, and the energy cascade rate should be redefined as an effective mean total energy cascade rate: $\epsilon_{eff} \equiv \epsilon + B_0^2 S/4$, and this will give us the necessary correction term in Equation (7).⁷ Performing the Taylor expansion of ϵ_{eff} in $v_{inj}/c_A < 1$ up to 2nd-order, the corrected sheet width can be written as:

$$\frac{\delta}{L} \simeq \min \left[\left(\frac{L}{l} \right)^{1/2}, \left(\frac{l}{L} \right)^{1/2} \right] \left[\frac{v_{inj}}{c_A} - C_2 \left(\frac{v_{inj}}{c_A} \right)^2 \right], \quad (9)$$

where C_2 is a coefficient resulting from the expansion. Figure 5 is the reconnection rates with various kinds of magnetization parameters: $\sigma = 0.04, 0.5, 1, 5$ which are fitted by 2 functions; one uses Equation (9) with the density ratio, Equation (6): $f(v_{inj}/c_A) = C_1(\rho_s/\rho_{in})[v_{inj}/c_A - C_2(v_{inj}/c_A)^2]$, and the other only takes into account the density ratio and uses LV99 sheet width, Equation (9): $g(v_{inj}/c_A) = C_1(\rho_s/\rho_{in})v_{inj}/c_A$. Note that C_1 and C_2 describe coefficients independent of the injection velocity v_{inj} indicated by Equation (9). As can be seen, they are well-reproduced only by f whose C_2 are around unity in all the cases.

The above discussion assumes that the turbulence becomes compressible. To conform the validity of this assumption, we performed the Helmholtz decomposition and the MHD wave mode decomposition of the velocity field. The analysis were

⁷ The source/sink term S from compressible effects includes (1) mode exchange between the compressible modes and Alfvén mode; (2) a direct cascade of eddy size by dilatation ($\nabla \cdot \vec{v} > 0$) or compression ($\nabla \cdot \vec{v} < 0$) (more detailed discussion can be found in (Banerjee & Galtier 2013)). It is our future work to determine which effect works dominantly.

performed using a background obtained by new runs without current sheets but using the same setup. This is because the current sheets introduce an inhomogeneous background which makes it very difficult to perform the above decomposition. The top panel of Figure 6 are the ratio between the compressible and incompressible velocity components: $\langle v_c^2 \rangle$ and $\langle v_i^2 \rangle$, respectively in terms of the Alfvén Mach number of the injected turbulence velocity dispersion, v_{inj}/c_A , using various magnetization parameter σ . As expected, this shows that in all cases the compressible component increases with the turbulent strength. We also note that the maximum reconnection rate in Figure 2 is obtained when $\langle v_c^2 \rangle / \langle v_i^2 \rangle \sim 0.4$. Interestingly, Figure 6 shows the compressible component increases with the magnetization of the plasma similarly to in non-relativistic MHD turbulence (Cho & Lazarian 2002). We consider this is due to the B_0^2 factor in Equation (8), which indicates the compressible effects becomes more important as the background magnetic field increases. Unfortunately, Equation (8) is a result in the case of the non-relativistic MHD turbulence, and its relativistic extension is our future work. The bottom panel of Figure 6 is the ratio of the fast MHD wave to the Alfvén wave power. The wave decomposition was performed in the Fourier space assuming the linear dispersion relation similarly to the non-relativistic case by Cho & Lazarian (2002). It shows a very similar behavior obtained by the Helmholtz decomposition. Interestingly, we also found the slope of the ratio, $(V_f/V_A)^2$, is proportional to $\sqrt{\sigma}$, so that it can be written as: $(V_f/V_A)^2 \propto \sqrt{\sigma} v_{inj}/c_A$. Equation (9) can effectively be derived by considering the wave decomposition. The turbulent reconnection theory in LV99 considers the MHD turbulence results in a wider current sheet because of the wandering motion of the magnetic field driven by Alfvén waves. Hence, ϵ_{inj} in Equation (7) is equivalent to the Alfvén wave power, V_A^2 , where V_A is the Alfvén wave component of the velocity. In the compressible regime, a part of injected energy is distributed into the fast wave, and ϵ_{inj} in Equation (7) should be rewritten as:

$$V_A^2 \simeq v_{inj}^2 - V_f^2 \sim v_{inj}^2 - V_A^2 \sqrt{\sigma} v_{inj}/c_A, \quad (10)$$

where V_f is the fast wave component of the velocity. This reduces to

$$\sqrt{V_A^2} \sim v_{inj} \left[1 - \frac{\sqrt{\sigma}}{2} \frac{v_{inj}}{c_A} \right], \quad (11)$$

where we assume $v_{inj}/c_A < 1$. This reproduces the dependence of Equation (11) on v_{inj} ⁸. However, we cannot find the dependence of C_2 on $\sqrt{\sigma}$ indicated by Equation (11). We consider this may be due to the effect of inhomogeneous background structure and the back reaction from the tearing instability which are not taken into account to obtain Figure 6.

5. APPLICATIONS TO HIGH ENERGY ASTROPHYSICAL PHENOMENA

In this section, we discuss applications to high energy astrophysical phenomena, that is, the Crab pulsar wind nebula, relativistic jets, and gamma-ray bursts. We estimate the necessary spatial and temporal scales for explaining those phenomena, and compare them with the actual observational indications. In those phenomena, it is natural to consider the driving source of turbulence depends on phenomena and

⁸ Note that slow waves basically propagate along magnetic fields, and they are also responsible for the magnetic field wandering.

the resulting turbulence strength is different. However, there are still a lot of theoretical and observational uncertainties in those phenomena, such as the precise spatial distribution of the magnetic field strength, the particle number density, and the particle composition which is necessary to estimate synchrotron radiation flux. And identifying each turbulent process is beyond the scope of this paper. Hence, in the following, we only use the values of reconnection rate to estimate those scales, so that the discussions can in general be applied for another dissipation mechanism, such as collisionless reconnection or plasmoid-chains.

–Crab Pulsar Wind Nebula

In the case of the Crab pulsar wind nebula, the wind region is filled with current sheets (*striped wind*). It is known that the magnetic field cannot be completely dissipated in the wind region (Lyubarsky & Kirk 2001; Kirk & Skjæraasen 2003). One way to avoid this problem is to assume that the magnetic field dissipates just behind the termination shock (Lyubarsky 2003; Pétri & Lyubarsky 2007; Sironi & Spitkovsky 2011). If assuming high- σ upstream flow, the down stream of the termination shock is still relativistic flow with Lorentz factor $\sqrt{\sigma}$. In the downstream rest frame, the sheet separation is around $\pi\sqrt{\sigma}r_{LC}$ where $r_{LC} = c/\Omega$ is the light cylinder radius, and Ω is the rotation period of the Crab pulsar. The necessary timescale to dissipate the magnetic field between the sheets by reconnection with reconnection rate v_{in} is $\pi\sqrt{\sigma}r_{LC}/v_{in}$. In the termination shock rest frame, which would be equivalent to the observer's frame, additional Lorentz factor $\sqrt{\sigma}$ is multiplied to the dissipation time scale, and it becomes

$$\tau_{\text{dissip,PWN}} = \pi\sigma r_{LC}/v_{in}. \quad (12)$$

During this timescale, the current sheets propagates

$$\begin{aligned} l_{\text{dissip}} &= c\tau_{\text{dissip,PWN}} = \pi\sigma r_{LC}c/v_{in} \\ &= 5 \times 10^{-5} [\text{pc}] \left(\frac{2\pi r_{LC}}{10^9 [\text{cm}]} \right) \left(\frac{\sigma}{10^4} \right) \left(\frac{v_{in}/c}{0.1} \right)^{-1}, \end{aligned} \quad (13)$$

which is sufficiently short compared to the Crab pulsar wind nebula scale size (~ 1 [pc]), and the turbulent reconnection can be one of the possible dissipation mechanisms to solve the σ -problem. The indicated value in Equation (13) is still too small to be resolved by X-ray (e.g. by the Chandra telescope). However, it may be possible to be observed by a future mission if σ is larger than 10^4 and the reconnection rate v_{in}/c is smaller than 0.1.

–Relativistic Jets

In this case, although there is no proof of the existence of current sheets in the observed jets, we assume a dynamo-process such as the magneto-rotational instability (MRI) in their accretion disk results in current sheets in jets (Barkov & Baushev 2011). Assuming the separation in the fluid comoving frame as \bar{l} , the reconnection timescale can be written as: $\bar{\tau}_{\text{dissip}} = \bar{l}/v_{in}$ in the fluid comoving frame. If we assume the reversing of the magnetic field direction occurs every one-Kepler rotation time at a radius r , the timescale in the blackhole rest frame can be written as, $\tau_{\text{rot}} \sim \pi r_M (2r/r_M)^{3/2}/c$ where r_M is the Schwarzschild radius. Hence, \bar{l} can be written as, $\Gamma_{\text{jet}} c \tau_{\text{rot}}$. Since the dissipation timescale in the central blackhole comoving frame, $\Gamma_{\text{jet}} \bar{\tau}_{\text{dissip}}$,

should be less than the jet propagation time, l_{jet}/c , we obtain

$$\begin{aligned} \frac{v_{in}}{c} &\gtrsim \frac{\bar{l}}{l_{\text{jet}}} \Gamma_{\text{jet}} \sim \pi \Gamma_{\text{jet}}^2 \left(\frac{r_M}{l_{\text{jet}}} \right) \left(2 \frac{r}{r_M} \right)^{3/2} \\ &\sim \begin{cases} 1.9 \times 10^{-3} \left(\frac{l_{\text{jet}}}{60 [\text{pc}]} \right)^{-1} \left(\frac{r}{3r_M} \right)^{3/2} \left(\frac{r_M}{10^{-4} [\text{pc}]} \right) \left(\frac{\Gamma_{\text{jet}}}{5} \right)^2 & (\text{radio}), \\ 3.3 \times 10^{-4} \left(\frac{l_{\text{jet}}}{0.5 [\text{kpc}]} \right)^{-1} \left(\frac{r}{3r_M} \right)^{3/2} \left(\frac{r_M}{10^{-4} [\text{pc}]} \right) \left(\frac{\Gamma_{\text{jet}}}{6} \right)^2 & (\text{HST}), \end{cases} \end{aligned} \quad (14)$$

where the upper and lower values are based on the radio and HST data of M87 (Rieger & Aharonian 2012). Here we assume the reversing of the magnetic field direction occurs at the innermost secure radius $r = 3r_M$. This indicates the both observation results can be explained by turbulent reconnection.

–Gamma Ray Bursts

It is suggested that GRB can be explained by Poynting-dominated plasma model, and Zhang & Yan (2011) suggested a model called ICMART model that can explain GRB including prompt emission spectral curves (Zhang & Zhang 2014). In the model, the reconnection rate is assumed a relativistic value, the minimal value is around $0.1c$. As indicated in Figure 2, this value of reconnection rate will be obtained by turbulent reconnection in Poynting dominated plasma. The model also discussed a possible role of reconnection outflow assuming Alfvénic velocity, $\gamma_A \sim \sqrt{1+\sigma}$. In our calculations, a relativistic outflow was observed only locally and intermittently; the averaged outflow velocity was a sub-relativistic velocity up to $\sim 0.3c$ even in the high- σ regime, which is commonly seen in the relativistic MHD reconnection resulted from the tearing instability. If we see a smaller scale, the collisionless plasma regime will appear in which the outflow velocity is Alfvén velocity in the high- σ regime (Liu et al. 2015).

Recently, Lazarian & Medvedev (2015) proposed a new scenario for the gamma-ray bursts powered by turbulent reconnection based on kink instability of relativistically magnetized jets (Mizuno et al. 2012). In this model, the authors considered a turbulence induced by the kink instability, and applied it to the turbulent reconnection model. They showed that their model can provide a good fit to the dynamics of GRBs. Note that this model may also be able to be applied to AGN jets, which may result in a different condition from Equations (14).

–General Remarks

Finally, we give several comments which can be applied to any phenomena in general if turbulent reconnection works. First, our results, such as the Figure 2, indicates that the maximum reconnection rate is obtained when $v_{inj}/c_A \sim 0.2$. Assuming the Alfvénic mode, $\delta B/B_0 \sim \delta v_{\perp}/c_A$, where B_0 and δB are the background and fluctuation of magnetic field, respectively, δv_{\perp} is the fluctuation velocity perpendicular to B_0 , we can expect that the turbulent reconnection is efficient if an observed magnetic fluctuation of some phenomena is around $\delta B \sim 0.2B_0$. In addition, we can expect that such a low magnetic fluctuation will allow a high polarization degree of synchrotron radiation observed by Coburn & Boggs (2003). Second, it is well-known that magnetic reconnection is also related to particle acceleration. For example, many Particle-In-Cell simulations indicates that the energy spec-

trum index obtained in relativistic collisionless pair-plasma reconnection is around -1.5 (Zenitani & Hoshino 2001; Bessho & Bhattacharjee 2012; Sironi & Spitkovsky 2014; Guo et al. 2015). On the other hand, de Gouveia dal Pino & Lazarian (2005) found that the turbulent reconnection is also a location of the first-order Fermi process, and they obtained a little softer energy spectrum index, -2.5 . Non-thermal particle energy index is directly related to the observed synchrotron spectrum, and the above energy spectrum index may be useful tool to determine the location of turbulent reconnection. Applications of turbulent reconnection model to some AGNs are provided in (Khiali et al. 2015; Kadowaki et al. 2015; Singh et al. 2015). More comprehensive discussion of recent observations is given in Lazarian et al. (2015).

6. DISCUSSION AND CONCLUSION

In this paper, we investigated turbulent reconnection in relativistic plasmas from the matter dominated to Poynting dominated cases using the relativistic resistive MHD model. The results show that the turbulence can enhance magnetic reconnection even in relativistic plasmas, and can be a candidate for a fast reconnection process. We found the reconnection rate in turbulence shows the following 3 characteristic phase depending on the velocity of the injected turbulence: (1) LV99 region (incompressible turbulence); (2) saturation region giving maximum rate; (3) reducing due to the compressibility. The saturation occurs when the compressible component become dominant, typically around $v_c^2/v_t^2 \gtrsim 0.4$ at which the maximum reconnection rate is about 0.05. This shows that the LV99 expressions for incompressible fluid should be modified to account for compressibility as we have done in Equations (6) and (9). Interestingly, Banerjee & Galtier (2013) showed that dilatation of fluid, $\nabla \cdot \vec{v} > 0$, reduces the effective energy cascade rate ϵ_{eff} . All of our numerical results showed dilatation, and the reconnection rates are indeed reduced. This indicates that the turbulent reconnection rate may become larger than LV99's prediction if compression of the turbulence occurs, such as the MHD turbulence driven by collisions of magnetized blobs (Inoue et al. 2011; Deng et al. 2015).

Finding a fast reconnection process is one of the most important topics in plasma physics, and a considerable number of studies have been conducted on it for a long time. Turbulence is a very general process in high-Reynolds number plasmas, so that turbulent reconnection can appear in many kinds of phenomena, such as astrophysical phenomena, nuclear fusion, and laser plasma. In particular, our work investigated the extension of turbulent reconnection to relativistic plasma with compressible turbulence, which allows us to apply this process to many high energy astrophysical phenomena, such as flares in pulsar wind nebulae, gamma ray bursts, and relativistic jets.

We would like to thank John Kirk, Sébastien Galtier, Supratik Banerjee for many fruitful comments and discussions. We also would like to thank our anonymous referee for a lot of fruitful comments on our paper. Numerical computations were carried out on the Cray XC30 at Center for Computational Astrophysics, CfCA, of National Astronomical Observatory of Japan. Calculations were also carried out on SR16000 at YITP in Kyoto University. This work is supported in part by the Postdoctoral Fellowships for Research Abroad program by the Japan Society for the Promotion of

Science No. 20130253 and also by the Research Fellowship for Young Scientists (PD) by the Japan Society for the Promotion of Science No. 20156571 (M.T.). One of the author (A. Lazarian) is supported by NSF AST 1212096. This work is also supported in part by Grants-in-Aid for Scientific Research from the MEXT of Japan, 15K05039 (T.I.).

REFERENCES

- Banerjee, S., & Galtier, S. 2013, *Phys. Rev. E*, 87, 013019
 Barkov, M. V., & Baushev, A. N. 2011, *New A*, 16, 46
 Begelman, M. C., Blandford, R. D., & Rees, M. J. 1984, *Reviews of Modern Physics*, 56, 255
 Bessho, N., & Bhattacharjee, A. 2012, *ApJ*, 750, 129
 Bhattacharjee, A., Huang, Y.-M., Yang, H., & Rogers, B. 2009, *Physics of Plasmas*, 16, 112102
 Biskamp, D. 1986, *Physics of Fluids*, 29, 1520
 Blandford, R. D., & Znajek, R. L. 1977, *MNRAS*, 179, 433
 Brunel, F., Tajima, T., & Dawson, J. M. 1982, *Physical Review Letters*, 49, 323
 Cho, J., & Lazarian, A. 2002, *Physical Review Letters*, 88, 245001
 Coburn, W., & Boggs, S. E. 2003, *Nature*, 423, 415
 de Gouveia dal Pino, E. M., & Lazarian, A. 2005, *A&A*, 441, 845
 Deng, W., Li, H., Zhang, B., & Li, S. 2015, *ApJ*, 805, 163
 Eyink, G. L. 2011, *Phys. Rev. E*, 83, 056405
 Galtier, S., Nazarenko, S. V., Newell, A. C., & Pouquet, A. 2000, *Journal of Plasma Physics*, 63, 447
 Goldreich, P., & Sridhar, S. 1995, *ApJ*, 438, 763
 Guo, F., Liu, Y.-H., Daughton, W., & Li, H. 2015, *ApJ*, 806, 167
 Higashimori, K., Yokoi, N., & Hoshino, M. 2013, *Physical Review Letters*, 110, 255001
 Hoh, F. C. 1966, *Physics of Fluids*, 9, 277
 Inoue, T. 2012, *ApJ*, 760, 43
 Inoue, T., Asano, K., & Ioka, K. 2011, *ApJ*, 734, 77
 Kadowaki, L. H. S., de Gouveia Dal Pino, E. M., & Singh, C. B. 2015, *ApJ*, 802, 113
 Kennel, C. F., & Coroniti, F. V. 1984a, *ApJ*, 283, 694
 —. 1984b, *ApJ*, 283, 710
 Khiali, B., de Gouveia Dal Pino, E. M., & del Valle, M. V. 2015, *MNRAS*, 449, 34
 Kino, M., Takahara, F., Hada, K., Akiyama, K., Nagai, H., & Sohn, B. W. 2015, *ApJ*, 803, 30
 Kirk, J. G., & Skjærraasen, O. 2003, *ApJ*, 591, 366
 Komissarov, S. S., Barkov, M. V., Vlahakis, N., & Königl, A. 2007, *MNRAS*, 380, 51
 Kowal, G., Lazarian, A., Vishniac, E. T., & Otmianowska-Mazur, K. 2009, *ApJ*, 700, 63
 Lazarian, A., & Medvedev, M. V. 2015, preprint
 Lazarian, A., & Vishniac, E. T. 1999, *ApJ*, 517, 700
 Lazarian, A., Kowal, G., Takamoto, M., de Gouveia Dal Pino, E. M., & Cho, J. 2015, preprint
 Liu, Y.-H., Guo, F., Daughton, W., Li, H., & Hesse, M. 2015, *Physical Review Letters*, 114, 095002
 Loureiro, N. F., Schekochihin, A. A., & Cowley, S. C. 2007, *Physics of Plasmas*, 14, 100703
 Lyubarsky, Y. 2010, *ApJ*, 725, L234
 Lyubarsky, Y., & Kirk, J. G. 2001, *ApJ*, 547, 437
 Lyubarsky, Y. E. 2003, *MNRAS*, 345, 153
 —. 2005, *MNRAS*, 358, 113
 Lyutikov, M., & Blandford, R. 2003, *ArXiv Astrophysics e-prints*
 Lyutikov, M., & Lazarian, A. 2013, *Space Sci. Rev.*, 178, 459
 Mac Low, M.-M. 1999, *ApJ*, 524, 169
 Matthaeus, W. H., & Lamkin, S. L. 1985, *Physics of Fluids*, 28, 303
 Meyrand, R., Galtier, S., & Kiyani, K. H. 2015, *ArXiv e-prints:1509.06601*
 Mizuno, Y., Lyubarsky, Y., Nishikawa, K.-I., & Hardee, P. E. 2012, *ApJ*, 757, 16
 Parker, E. N. 1957, *J. Geophys. Res.*, 62, 509
 Perez, J. C., & Boldyrev, S. 2008, *ApJ*, 672, L61
 Pétri, J., & Lyubarsky, Y. 2007, *A&A*, 473, 683
 Rieger, F. M., & Aharonian, F. 2012, *Modern Physics Letters A*, 27, 30030
 Shibata, K., & Tanuma, S. 2001, *Earth, Planets, and Space*, 53, 473
 Singh, C. B., de Gouveia Dal Pino, E. M., & Kadowaki, L. H. S. 2015, *ApJ*, 799, L20
 Sironi, L., & Spitkovsky, A. 2011, *ApJ*, 741, 39
 —. 2014, *ApJ*, 783, L21

- Sweet, P. A. 1958, in IAU Symposium, Vol. 6, Electromagnetic Phenomena in Cosmical Physics, ed. B. Lehnert, 123
- Takahashi, H. R., Kudoh, T., Masada, Y., & Matsumoto, J. 2011, ApJ, 739, L53
- Takamoto, M. 2013, ApJ, 775, 50
- Takamoto, M., & Inoue, T. 2011, ApJ, 735, 113
- Takamoto, M., Inoue, T., & Inutsuka, S. 2012, ApJ, 755, 76
- Uzdensky, D. A., Loureiro, N. F., & Schekochihin, A. A. 2010, Physical Review Letters, 105, 235002
- Verdini, A., & Grappin, R. 2012, Physical Review Letters, 109, 025004
- Zenitani, S., & Hoshino, M. 2001, ApJ, 562, L63
- Zhang, B., & Yan, H. 2011, ApJ, 726, 90
- Zhang, B., & Zhang, B. 2014, ApJ, 782, 92